Microcoil MRI of plants and algae at ultra-high field : an exploration of metabolic imaging

Schadewijk, R. van

1 GENERAL INTRODUCTION

Society has a pressing need for sustainable food and energy production, as well as halting any further environmental degradation by human activity, to avert catastrophic changes to the global climate (IPCC 2014). Central to many of challenges facing humanity, such as food and energy security, are metabolic processes. The metabolism of an organism is dependent on and shaped by its environment. For multi-cellular organisms, the anatomy plays a role as well, and the interactions of metabolism tissue function may be collectively described as physiology. The intricacies of the metabolism take many shapes, whether it be through tissue specialisation in the form of organs, *e.g.* root nodules in *M. truncatula*, or concentration gradients of nutrients or metabolic intermediates (Nap and Bisseling, 1990; Xiao *et al.*, 2014; Pfau *et al.*, 2016). Understanding the processes within organisms may potentially aid in answering challenges facing humanity, related to energy and food security.

Metabolic profiling and metabolomics are a long-standing tradition in plant biology, due to the strong relation of metabolism with plant growth. Over the past decades, several advanced techniques have become available including gas chromatography (GC), liquid chromatography (LC), mass spectroscopy (MS) and their combinations: GC-MS, LC-MS and GC-LC (Barsch *et al.*, 2006; Sumner *et al.*, 2014). Since metabolic profiles can vary across tissues, there is a need to visualise metabolic profiles using localised techniques. Surface mapping of metabolites is possible with techniques such as mass spectroscopy imaging (MSI) and surface-enhanced Raman spectroscopy (Ye *et al.*, 2013; Boughton *et al.*, 2016; Espina Palanco, Mogensen and Kneipp, 2016). While the described techniques are capable of resolving many metabolites, sample material must frequently be pooled in order to obtain sufficient quantities of material and imaging is mostly restricted to surface tissue. In contrast, MRI is a 3D imaging technique based on detecting nuclear spin, capable of resolving tissue anatomy and metabolic profiles *in-vivo* or *in-situ*, though MRI is typically less sensitive compared to other techniques. In many applications, the previously mentioned techniques may be used in combination with NMR or MRI to complement each other.

This thesis uses a flexible approach to apply the latest development in MRI to two model systems, *B. braunii* and *M. truncatula*. These model systems were selected based on their importance for research for a sustainable society (Barker *et al.*, 1990; Metzger and Largeau, 2005; Tasić *et al.*, 2016). In order to map the variation of metabolic profiles across tissues, Magnetic Resonance Imaging (MRI) is used extensively, due to its ability to non-invasively study both anatomy and spectroscopy (Van As and van Duynhoven, 2013). MRI methodology was developed for these applications, through protocol development, coil selection and home-built microcoils for ultra-high field strengths.

1.1 THEORY OF MAGNETIC RESONANCE IMAGING

Nuclear Magnetic Resonance is made possible by a property of nuclei called spin. NMR was first observed experimentally in independent studies by Purcell and Bloch in 1946

(Bloch, 1946; Purcell, Torrey and Pound, 1946). NMR instruments are capable of revealing detailed information on the nuclear spins contained in a sample. These spins are manipulated using a combination of strong magnetic fields and radiofrequency pulses. The origin of spin can be described accurately by quantum mechanics (Levitt, 2001). Only nuclei with an uneven number of protons or neutrons exhibit spin. For instance, hydrogen (^{1}H) contains only one proton and has spin $S = ½$, and its isotope deuterium (^{2}H) has one proton and one neutron and has spin $S = 1$. Spin is interesting as a physical property because it has no clear parable in daily life, *e.g.*, like an apple falling from a tree, such as in the case of gravity. However two useful analogies may be found to aid in understanding spin, the first being a bar magnet, and the second is that of a children's spinner toy (rotational motion).

The first analogy, a bar magnet, helps explain the reaction of nuclear spin to an external magnetic field (B), measured in Tesla (T). In the absence of a magnetic field, the orientation of the spin of nuclei is randomly distributed. In other words, the energy levels are degenerate, see Fig. 1.1. However, when an external magnetic field is applied, the energy levels of the quantified spins split.

The number of possible spin states depends on the type of nucleus. Here we consider only the spin-½ nuclei of hydrogen (^{1}H). In the case of spin-½, the spins are either parallel or anti-parallel to the external field, and the lowest state is with the spins parallel to the applied field, similar to how a bar magnet aligns parallel to an external magnetic field (Fig. 1.1). Note that the bar magnet analogy is a simplified interpretation of the quantum mechanical nature of spin. In fact, spin can exist in any linear combination of the + ½ and – ½ states. For a detailed description, see Levitt (2001).

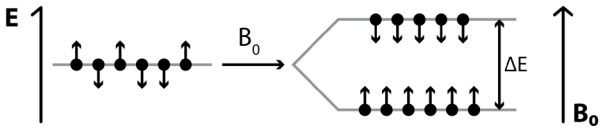

Fig. 1.1 Orientation of spin in spin-½ nuclei, in response to an external static magnetic field (B_0). In the initial state, the spins are randomly distributed over the + ½ and – ½ states. When the magnetic field is applied, the nuclei orient themselves in one of two possible directions: parallel to the magnetic field, or antiparallel. The parallel orientation is very slightly more energetically favoured than the antiparallel state. This minute difference means slightly more spins are oriented parallel to the field. Note that this model is a simplified interpretation of the quantum reality of spin.

There is a slight preponderance for spins to align parallel to the field, which is crucial as this difference can be used to excite to an observable magnetisation. The energy difference depends on the magnet field strength B_0. (Eq. 1.1).

$$\Delta E = \gamma \hbar B_0 \tag{1.1}$$

Where $\hbar$ is the reduced Plank constant ($h/2\pi$), and γ is the gyromagnetic ratio of the specific nucleus in question. The ratio of parallel vs anti-parallel spins follows the Boltzmann distribution (Eq. 1.2):

$$\frac{N_{\mathrm{ap}}}{N_{\mathrm{p}}} = e^{-\frac{\Delta E}{kT}} \tag{1.2}$$

Where N_{ap}/N_p is the ratio of parallel vs anti-parallel spins, ΔE represents the energy difference described by Eq. 1.1, T is the temperature in Kelvin, and k is the Boltzmann constant.

The excess spins in the parallel state represent a small fraction, roughly around 1 in 10^4 spins under an ultra-high field strength of 22.3 T. This small polarisation means that NMR is an inherently low sensitivity technique, but due to the considerable amount of spins in a typical sample, there is still sufficient signal to detect. The magnetisation can be represented by a vector, containing both magnitude and direction of the magnetisation. By convention, the direction of the magnetic field lies along the Z-axis.

The second analogy is that of a spinner toy. Normally, when spun, a spinner will try to remain upright as it tries to retain angular momentum. When the spinner is perturbed, for example by a gentle nudge, its angular momentum gives rises to an unusual phenomenon called precession. Precession is the tendency to resist changes to an object's momentum by rotating around its axis in a manner depicted in Fig. 1.2A. Nuclei with spin react in the same way as a spinner or gyroscope when forced out of balance; they too will precess. When discussing precession, it is easier to use a rotating frame of reference, where the X and Y axes spin at the same frequency (ω) as the vector of interest. A vector with the same precession frequency (ω) appears to be static in the rotating frame (Fig. 1.2B).

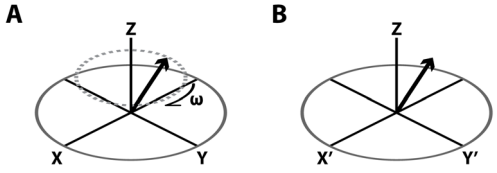

Fig. 1.2 The precession phenomenon. (A) A vector is used to represent precession with an arbitrary frequency (ω) around the z-axis. **(B)** A useful tool to work with precession is the rotating frame, where the X-axis and Y-axis rotate at the same frequency (ω) as the precession of interest. The rotating frame axes are denoted with X′ and Y′ respectively. The rotating frame results in a vector that appears static in the rotating frame.

1.1.1 MAGNETISATION

In summary, spin combines some properties of angular momentum and magnetism. The polarisation due to excess spins in the parallel orientation (Z-direction) along a magnetic field, results in a magnetisation that can be represented as a vector. If the spins are perturbed, this vector will start to precess in the XY-plane (Fig. 1.2). It turns out that the precession frequency (ω) depends on the strength of the magnetic field, which is described by the Larmor equation (Eq. 1.3):

$$\omega = \gamma B_0 \tag{1.3}$$

For ^{1}H, the gyromagnetic ratio (γ) is 42.57 MHz T^{-1}, which is the highest of all nuclei, and B_0 is the magnetic field strength in Tesla. For a 17.6 T magnet, this results in a resonance frequency of 750 MHz. Generally, superconducting magnets are used to achieve high field strengths. Conveniently, the natural abundance of hydrogen is almost 100%, which combined with the high concentration of hydrogen nuclei in biological tissues, means hydrogen is the predominate nucleus used for NMR (Plewes and Kucharczyk, 2012).

In order to perturb or excite the spins, a secondary transient magnetic field in the rotating frame is used. This magnetic field can be generated with a radiofrequency (RF) pulse at the resonant frequency, *e.g.*, 750 MHz. The RF pulse flips the magnetisation to the XY- or transverse plane. The flip angle (α) can be by controlled by varying the duration of the RF pulse (Eq. 1.4).

$$\alpha = \gamma B_1 \tau \tag{1.4}$$

Where τ is the duration of the pulse and B_1 is RF pulse field strength.

Using RF receiving coils, also called resonators, the magnetisation in the transverse plane can be detected, and consequently, Fourier transformed to analyse the sample. Manipulating nuclear spin magnetisation with RF pulses is the basis of nuclear magnetic resonance (NMR) and gives rise to a wide variety of pulse schemes to investigate various aspects of samples of interest.

1.1.2 LONGITUDINAL AND TRANSVERSE RELAXATION

Immediately after a sample is excited using an RF pulse, it will start to relax back to its equilibrium state with all the magnetisation pointing along the z-direction. This return to equilibrium is called longitudinal relaxation. The decay of magnetisation is exponential and governed by equation 1.5:

$$M_Z(t) = M_{Z,0}\left(1 - e^{-\frac{t}{T_1}}\right) \tag{1.5}$$

Where $M_{Z,0}$ is the equilibrium state, and T_1 controls the rate of decay. T_1 is defined as the point in time where e^{-1} or ~63% of magnetisation has relaxed to equilibrium (Fig. 1.3A).

The evolution of magnetisation following an initial 90° RF pulse is shown graphically in Fig. 1.3B.

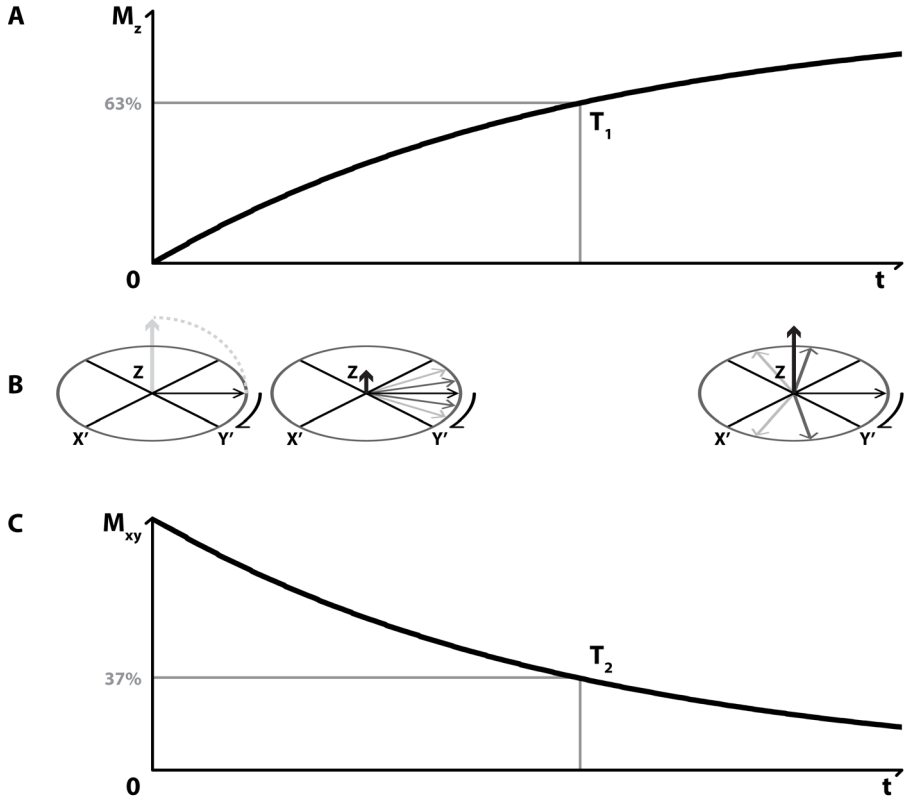

Fig. 1.3 T_1 and T_2 relaxation. (A) Longitudinal or T_1 relaxation. After an initial 90° excitation pulse, longitudinal magnetisation recovers exponentially. At T_1, approximately 63% of M_z magnetisation has recovered. **(B)** Graphical representation of T_1 and T_2 relaxation. The initial state depicts a 90° pulse flipping full magnetisation in the transverse (XY) plane. Next, the resonance evolves progressively until near complete relaxation. A thick black vector indicates longitudinal magnetisation, while arrows in the XY-plane depicts transverse dephasing due to different resonant frequencies. **(C)** Graph of transverse or T_2 relaxation. Due to differences in resonance frequencies, over time spins dephase which destroys the coherence of the signal. Similar to T_1, T_2 is defined as the time were 37% of the transverse magnetisation remains.

A second mechanism termed transverse or T_2 relaxation causes loss of magnetisation in the XY-plane. Transverse relaxation is due to spin dephasing, caused by a difference in resonant frequency of the spins in the sample, see Fig. 1.3B. Because individual spins cannot be detected, only the summation of all spins, loss of coherence results in loss of detectable signal. Like longitudinal relaxation, transverse relaxation is an exponential process:

$$M_{XY}(t) = M_{XY,0} e^{-\frac{t}{T_2}} \quad (1.6)$$

Where $M_{XY,0}$ is the magnetisation immediately after excitation, and T_2 is the duration of time when e^{-1} or 63% of total magnetisation has been relaxed (Fig 1.3C). Local field inhomogeneity caused by imperfections in the B_0 field or local differences in susceptibility, *e.g.*, air-water transitions, can cause the signal to relaxer faster than predicted by Eq. 1.6. The actual observed T_2 is termed T_2*. Some strategies are used to mitigate signal loss due to T_2* effects, such as the spin echo sequence. In spin echo sequences the evolution of spins is reversed by applying a 180° pulse. This 180° pulse reverses the direction of all spins, to refocus the T_2* induced changes.

Both T_1 and T_2 relaxation occur simultaneously, but typically the T_1 is much longer (in the order of seconds) than the T_2 (in the order of milliseconds).

1.1.3 MAGNETIC RESONANCE IMAGING: SPATIAL ENCODING

When an RF pulse excites a sample within an NMR instrument, typically a signal arising from the entire sample is detected. If one wants to use the NMR phenomenon to create images, this signal needs to be localised. Magnetic Resonance Imaging (MRI) is able to achieve localisation by employing transient magnetic fields, whose strength varies depending on location. These magnetic fields are generated by supplying current to loops of wires that can generate linear magnetic field gradients in three orthogonal directions (X, Y, Z). These fields result in the resonance frequency becoming linearly dependent on the position of the nuclei within the sample holder. For successful imaging, the signal has to be localised in all three dimensions. Three approaches may be used to achieve this, generally in the following order: slice selection, phase encoding and frequency encoding.

Slice selection is often used as the first step in localising the NMR signal. Simultaneously with an RF pulse, a magnetic gradient is applied, resulting in the selection of a slice of spins within the sample. Figure 1.4A indicates the overlap of RF bandwidth and the frequency range within the sample.

Encoding of the second dimension is done using phase encoding. By applying a magnetic gradient along, for example, the Y-axis, spin precession speeds up or slows down, depending on the location of the spins in the magnetic field (Fig. 1.4B). When the magnetic field gradient is released, the spin precession frequencies return to normal, but the phase of the spin will either lead or trail the reference spin phase at the centre of the coils. Thus information on the location of spins in the Y-dimension has been encoded in their phase angle. For each line in an image, the strength of the phase encoding gradient may be increased.

Spatial information on the last dimension can be obtained through frequency encoding (Fig. 1.4C). The signal is recorded or 'sampled' multiple times during signal acquisition, while a gradient is active in the Z-dimension. The frequency of spins within the sample

thus continuously evolves between each sampling point. The rate of change of spins between these sampling points then reveals the position of the spins along the Z-axis.

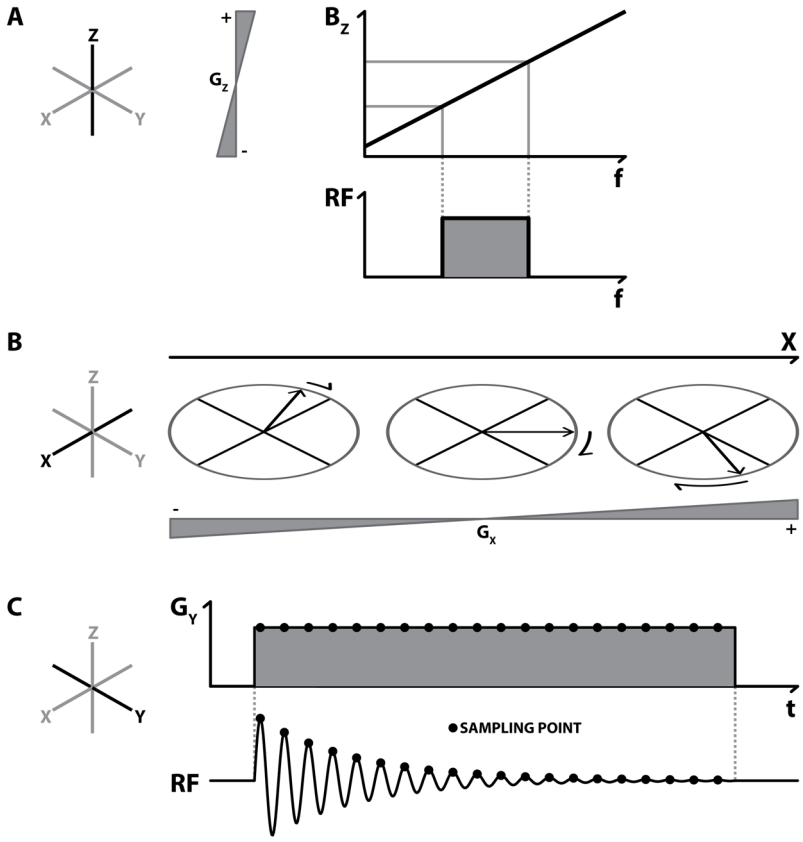

Fig. 1.4 Spatial encoding techniques of MRI. (A) Slice selection is achieved by applying a magnetic field gradient (shown here for the Z-axis), which makes the resonant frequency dependent on the position along the Z-axis. Simultaneously, an RF pulse is given, resulting in the excitation of spin polarisation with frequencies matching the RF pulse bandwidth. Thus a slice of spins is selected within the sample. **(B)** Phase encoding occurs using a gradient in an orthogonal direction to that of the slice selection, here the X-axis. This results in spin frequencies increasing or decreasing depending on their location. Once the gradient ends, the temporary frequency differences are retained as corresponding differences in the phase of spins. The phase encoding is varied for each line of an image. The strength of phase encoding depends on the strength and duration of the gradient. **(C)** Frequency encoding occurs when a signal is sampled multiple times while a gradient is active along the Y-axis. The gradient causes the frequency to evolve continuously while the signal is sampled. The localisation of the signal may then be reconstructed using Fourier transforms on the phase and frequency encoding directions (Plewes and Kucharczyk, 2012).

1.1.4 LOCALISED SPECTROSCOPY: VOLUME SELECTION

A localised NMR spectrum may be acquired by successive application of slice selection in all three dimensions. When implemented as a spin echo sequence, based on pulses

with a 180° flip angle, magnetisation is refocused in a three-dimensional volume of interest (VOI) at the intersection of three slice selective pulses.

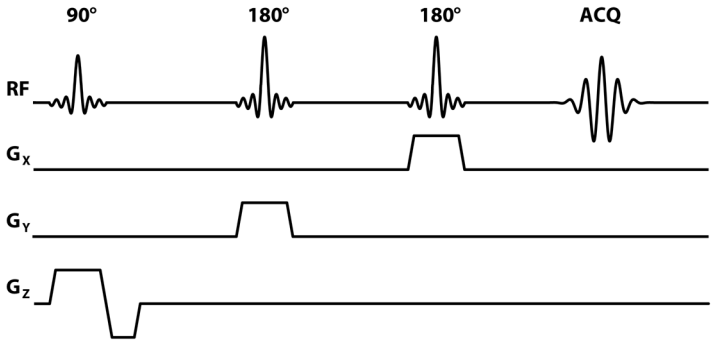

Fig. 1.5 Pulse sequence diagram of Point RESolved Spectroscopy (PRESS). A 90°-180°-180° pulse train coupled with simultaneous mutually orthogonal gradients selects a rectangular volume of interest. A localised spectrum is then obtained (Bottomley, 1987).

Figure 1.5 shows a pulse sequence diagram where each gradient is applied in a different plane, thus selecting a VOI. Only the VOI experiences all three (re)focusing pulses, all other areas receive only one or two pulses and are thus dephased by the time of signal acquisition. While PRESS results in a 1D spectrum, originating from the VOI, its volume selecting properties may also be used as the basis for more advanced pulse sequences.

1.1.5 DIFFUSION WEIGHTED IMAGING

MRI may also be used to investigate diffusion occurring within biological tissue (Luypaert *et al.*, 2001). Spatial encoding depends on the assumption that the nuclei-containing molecules remain static. This assumption, however, breaks down on a microscopic level because the molecules containing spins are subject to Brownian motion and depending on their local environment, free to diffuse (Le Bihan *et al.*, 2006). The assumption also breaks in the case of convection within samples, *e.g.*, transport of fluids in veins and channels. These phenomena can be used to reveal valuable information. In the case of diffusion, one can dephase spins using a gradient, and after an evolution time to allow for diffusion, rephase spins with an inverse gradient (Fig. 1.6A). For spin echo sequences, a Stejskal-Tanner type sequence with a gradient on either side of a 180° pulse is often used (Stejskal and Tanner, 1965). If a molecule experiences little diffusion, it will be in the same VOI when the second gradient is applied (Fig. 1.6B). The amount of phase encoding is, therefore, the same and its signal is not attenuated. However, a molecule that experiences strong diffusion will have moved in the time (Δ) between the two gradients. Since the molecule has moved, it will experience a different gradient strength in its new location. The result is a net signal attenuation that depends proportionally on the distance travelled.

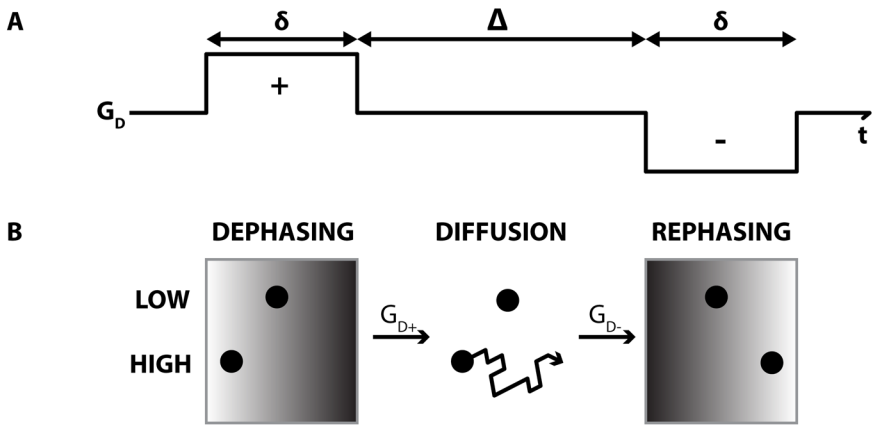

Fig. 1.6 Diffusion weighting using twin diffusion sensitising gradients. (A) A pair of gradients with the same strength and duration (δ), but inverse polarity, is used to attenuate the signal from molecules exhibiting high rates of diffusion selectively. The strength of the diffusion encoding depends on the strength and length of the gradients as well as an evolution time (Δ) between the gradients. **(B)** Graphical representation of diffusion. A particle with little diffusion moves a negligible amount between the two gradient pulses. Since it experiences the same amount as dephasing and rephasing, no signal attenuation takes place. In contrast, a high diffusion particle will move in between the two sensitising gradients and thus experience a net positive amount of dephasing. This dephasing results in signal attenuation that may be used to calculate an apparent diffusion coefficient (ADC).

An apparent diffusion coefficient (ADC) can be calculated using two or more images acquired with different diffusion weighting. The ADC is useful since it is a global statistical parameter that can be readily calculated for experimental measurements, in contrast to the underlying physical diffusion parameter *D*, which is difficult to determine experimentally (Le Bihan *et al.*, 2006). The ADC depends on experimental conditions such as voxel size or gradient duration, which can make it difficult to compare across different experiments. The strength of the diffusion weighting may be expressed as B-values (s mm^{-2}). The B-value is a convenient measure to express the total strength of the diffusion encoding experienced by a given molecule during the experiment. High B-values may be attained by strong gradients, long gradient durations or long gradient separation duration, or any combination thereof.

1.1.6 DIFFUSION WEIGHTED CHEMICAL SHIFT IMAGING DW-CSI

Several of the techniques described here may be combined in a modular approach that results in a sequence combining spatial localisation of spectroscopic information with diffusion weighting. The resulting sequence, Diffusion Weighted Chemical Shift Imaging (DW-CSI), is voxel-based with a 90°-180°-180° PRESS pulse train, see Fig. 1.7 (Ercan *et al.*, 2015). A slice selective gradient accompanies each radiofrequency (RF) pulse. Here shown as G_Z for the 90° pulse. Each consecutive 180° pulse has a slice selective gradient applied in an orthogonal direction, G_Y or G_X.

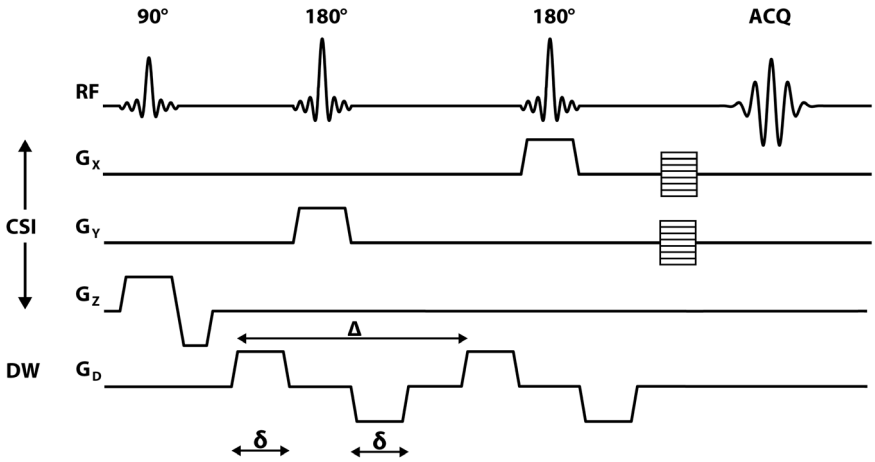

Fig. 1.7 DW-CSI Sequence Diagram. Radiofrequency pulses and resulting echo are shown on the top line. Chemical shift encoding is performed by a series gradients, shown here with G_Z fixed and increments in G_X and G_Y for each matrix position. Diffusion gradient, G_D, is shown separate from the CSI gradients, but in practice is intertwined with $G_{X,Y,Z}$ in any direction chosen at will. Diffusion sensitising strength is determined by the gradient separation (Δ), multiplied by the gradient duration (δ) and gradient strength.

The net result is efficient refocusing of magnetisation as an echo during acquisition (ACQ), within the intersection of slice gradients. The gradient directions may be chosen freely, so long as the gradients are mutually orthogonal. In contrast to regular imaging, CSI omits the readout gradient found in typical imaging sequences. Diffusion weighting is incorporated into the sequence by applying bi-polar diffusion sensitising gradients, centred around the two 180° pulses. The bi-polarity helps to avoid cross terms between the localising gradients and the diffusion sensitising gradients. For ease of comprehension, the diffusion weighting gradients (G_D) have been depicted separately from the main CSI sequence (Fig. 1.7). The diffusion gradients are interleaved with the main CSI sequence and can be applied in any primary direction or mixture thereof. For the sake of simplicity, the VAPOR water suppression immediately preceding the sequence has also been omitted.

1.1.7 MAGNETIC RESONANCE MICROSCOPY

Magnetic Resonance Microscopy (MRM) is defined as imaging at resolutions below 100 µm (Glover and Mansfield, 2002). High-resolution imaging requires high sensitivity since the experimental signal-to-noise ratio (SNR) scales linearly with the voxel volume, *i.e.*, $SNR \propto 1/{D_{\mathrm{voxel}}}^3$. An increase in resolution from 20 µm isotropic resolution ($20 \times 20 \times 20$ µm^3) to 10 µm isotropic resolution would decrease the voxel SNR by a factor 8. If one wishes to retain the same SNR as the lower resolution image, one could increase the number of measurements, since the SNR scales with the root of the number of experiments ($SNR \propto \sqrt{N_{\mathrm{exp}}}$). Thus, measurement time would need to be 64 times longer, which illustrates the importance of maximising the SNR via other means.

In order to maximise the experimental SNR, it is useful to investigate the contribution of different factors with a simplified equation for the SNR expressed in observed voltage (G. Webb, 1997; Webb, 2012):

$$SNR \propto [\gamma B_0]\left[\frac{\gamma^2 h^2 B_0 N_s}{16\pi^2 k T_S}\right]\left[\frac{B_1}{I}\right]\left[\frac{1}{V_{noise}}\right] \quad (1.7)$$

Here h is Plank's constant, N_s is the number of spins per volume, k is Boltzmann's constant, T_S is the sample temperature, B_1/I is the magnetic field strength generated per unit current, V_{noise} is the total voltage noise, including sample and circuity noise. The simplified equation may be broken down into four terms. The first term describes the relation of the induced voltage to the magnetic field flux (B_0). The second term describes the total magnetisation within the sample, which depends on the number of spins (N_s), field strength and temperature of the sample. Both the first and second term depend on B_0. SNR scaling with respect to B_0 has been reported in the literature as $B_0^{3/2}$ or $B_0^{7/4}$ (Hoult and Richards, 1976; Nakada, 2007; Webb, 2012). This dependence has driven the development of increasingly high field strengths, with pre-clinical MRI instruments of up to 22.3T in use. However, under ultra-high field conditions, the experimentally measured SNR correlation is approximately linear (Schepkin, 2016). The third term, B_1/I, describes the relation of SNR to the coil sensitivity, which has resulted in the creation of a broad range of coil geometry types and optimised coil designs (Fratila and Velders, 2011). Lastly, the fourth term, V_{noise} corresponds to the noise voltage, which itself consists of:

$$V_{noise} = \sqrt{4kT_C \Delta f R} \quad (1.8)$$

Where T_C is the temperature of the RF coil, Δf is the receiver bandwidth, and R is the resistance of the coil. The temperature dependence means that the noise voltage may be reduced by cooling the resonator and pre-amplifiers. In particular, cooling of both RF coils and pre-amplifier in cryoprobes results in SNR gains with a factor 3-4 (Kovacs, Moskau and Spraul, 2005). The insulation required between the sample, the coil and the instrument, poses significant technical challenges, increasing the complexity of cryogenic coil designs (Koo *et al.*, 2011).

MRM is made possible by using the three approaches of increasing field strength, optimised coil design and cooling RF circuitry, either separately or in conjunction with each other. Here, we focus on miniaturised coils or microcoils for use in ultra-high field spectrometers.

1.1.8 MICROCOILS

The highest possible image resolutions (up to 3 µm isotropic) have been attained with very small resonators called microcoils, with diameters (D_{coil}) in the mm to µm range (Ciobanu, Seeber and Pennington, 2002; Weiger *et al.*, 2008). Microcoils owe their sensitivity to the inverse scaling of SNR with coil diameter. The SNR of a solenoid

resonator increases as the diameter decreases with $1/D_{\mathrm{coil}}$. Below roughly 1mm in coil diameter, the sensitivity of microcoils scales with $1/\sqrt{D_{\mathrm{coil}}}$ (Peck, Magin and Lauterbur, 1995; Glover and Mansfield, 2002). Thus, coil design must closely match the sample size to ensure the highest achievable sensitivity. The ratio between sample volume and coil volume is termed the coil filling factor (*η)*.

Several types of coil design exist, including Helmholtz, saddle, birdcage, planar, stripline and solenoid coils design (Fratila and Velders, 2011). Solenoid coils are used extensively for MRM since they combine high sensitivity, homogeneous B_1 fields and ease of construction. The solenoid microcoil consists of a conducting wire wrapped around a capillary in the form of a helix (Fig. 1.8). The solenoid wire may be wound by hand, and the circuitry can be hand-soldered. Due to these properties, solenoid coils were selected for use in this thesis.

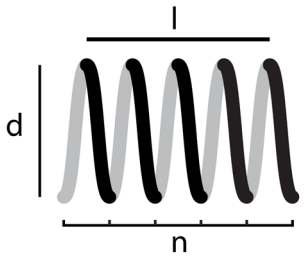

Fig. 1.8 Diagram of the solenoid coil and its measures. The dimensions of a solenoid coil are determined by its diameter (*d*), length (*l*) and the number of turns (*n*).

Like all NMR coils, microcoils operate by the principle of induction. The NMR phenomenon induces a voltage oscillation in a resonant circuit, consisting of the coil and a capacitor. Though radiofrequency pulses are used, NMR is not a radiofrequency spectroscopic technique since the signal observed in detection coils is caused by induction, with radio waves playing a negligible role (Hoult, 2010).

The sensitivity per unit of current (B_1/I) of a solenoid resonator may be approximated with the following equation (Minard and Wind, 2001) :

$$\frac{B_1}{I} = \frac{\mu n}{d\sqrt{1 + \left(\frac{l}{d}\right)^2}} \tag{1.9}$$

Where μ_0 is the permeability of free space, *n* is the number of turns, *d* is the diameter of the coil and *l* is the length of the coil. If the ratio of length over diameter is kept constant, the sensitivity increases linearly as the coil diameter decreases. A higher number of turns also increases sensitivity, but the number of turns must be reduced as B_0 increases in order to avoid self-resonance on frequencies that interfere with the coil operating

frequency (Subramanian, Lam and Webb, 1998). The resonance frequency depends not only on the geometry of the coil, which determines the inductance, but also the capacitance of the circuit. In its simplest form, a resonator consists of an inductor (L) placed in parallel with a capacitor (C) to form a circuit (Fig. 1.9).

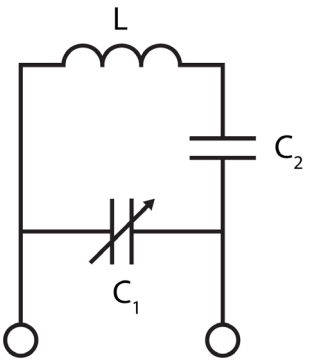

Fig. 1.9 Electrical Diagram of solenoid microcoil. The windings of the solenoid coil function as an inductor (L), while capacitors C_1 and C_2 are placed in series, parallel to the coil. C_1 often has a variable capacitance to allow for tuning.

The conditions for resonance are met if the reactance of L and C are equal (Wheeler and Conradi, 2012). Since inductive reactance increases with frequency while capacitive reactance decreases with frequency, there is a resonant frequency where inductance and capacitance are equal (Eq. 1.10):

$$\frac{\omega^2 LC}{2\pi} = 1 \tag{1.10}$$

Which leads to the resonance frequency:

$$\omega = \frac{1}{2\pi\sqrt{LC}} \tag{1.11}$$

By choosing an appropriately sized capacitor (C_1), the resonant frequency may be adjusted to obtain the required operating frequency. If a variable capacitor is used for C_1, it may be used for tuning of the resonant frequency. A capacitor (C_2) is placed in series with the coil, allowing the microcoil to be matched to 50 Ω by reducing the impedance of the circuit (Subramanian, Lam and Webb, 1998).

1.2 BIOFUELS DERIVED FROM ALGAE: *B. BRAUNII*

In the context of renewable energy, biodiesel is often considered, due to its potential to replace fossil fuels without major changes to fuel infrastructure or engines, for instance

in aviation (Kandaramath, Yaakob and Binitha, 2015; Yilmaz and Atmanli, 2017). Biodiesel may be derived from a variety of biomass sources, but algae are of particular interest due to their lack of competition with food production since no arable land is required for cultivation (Chisti, 2008; Benemann, 2013).

Botryococcus braunii has a global distribution and is found in brackish and freshwater environments (Wake and Hillen, 1980; Aaronson *et al.*, 1983; Metzger and Largeau, 2005). The high fraction of hydrocarbons present in *Botryococcus braunii* has attracted much attention, as they can be transformed into biodiesel (Hillen *et al.*, 1982; Eroglu and Melis, 2010; Demirbas and Fatih Demirbas, 2011). *B. braunii* accumulates high concentrations of oil as part of its normal life cycle, which may be improved by changing (stress) conditions, *e.g.* nitrogen deficiency (Al-Hothaly *et al.*, 2016; Cornejo-Corona *et al.*, 2016). Because of the relevance to biofuels, considerable effort has been spent on characterising *B. braunii* oils (Metzger *et al.*, 1985; Huang and Poulter, 1989; Sato *et al.*, 2003). Several strategies for oil extraction are currently available, with new possibilities being sought to extract oil without compromising colony viability (Furuhashi, Hasegawa, *et al.*, 2016). Attention has been given to the interaction of solvents with the colony exterior (Furuhashi, Noguchi, *et al.*, 2016). The lack of success in commercialisation of biofuels derived from *B. braunii* is attributed to its slow growth (Cabanelas *et al.*, 2015; Gouveia *et al.*, 2017). The slow growth itself may be correlated with the accumulation of hydrocarbons due to negative feedback (Banerjee *et al.*, 2002). More detailed understanding of the influence of oil on colony structure and growth is therefore desirable.

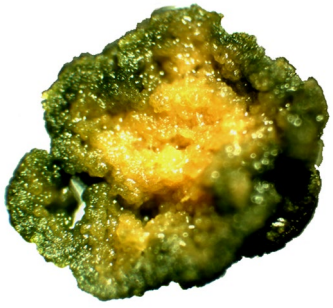

Fig. 1.10 Optical microscopy of a single *Botryococcus braunii* var. *showa* colony. The colony has been cut across, revealing the interior that displays an orange hue due to carotenoids. The background has been digitally removed. Image reproduced courtesy of Tomas van der Berg.

Botryococcus braunii exhibits a range of different metabolites depending on its race and strain. Here, the Race B variety *showa* (Berkeley strain) is studied exclusively (Fig 1.10). Since oil plays a central role in the morphology of *B. braunii*, we are interested in its influence on the diffusion of metabolites within the colony. MRI is used to study whole colonies non-invasively, combining imaging of their structure with metabolite mapping and diffusion measurements.

1.3 ROOT NODULATION IN *MEDICAGO TRUNCATULA*

Nitrogen plays a central role in biological processes, being a crucial component of DNA, RNA and the amide backbone of proteins. Bio-availability of nitrogen is, therefore, an essential factor determining the growth rate of plants. Nitrogen is mainly present in the atmosphere in its gaseous form (N_2), in which a strong triple bond binds two nitrogen atoms. Plants can only utilise nitrogen in organic forms, but the strength of the triple bond makes it energetically costly for plants to fix nitrogen from the air. Instead, through a remarkable feat of co-evolution, plants have effectively outsourced nitrogen fixation to a collection of metabolic symbionts, which includes arbuscular mycorrhizae and rhizobacteria (Bonfante and Genre, 2008; Suzaki, Yoro and Kawaguchi, 2015). These symbionts provide the plant with fixed nitrogen in return for nutrients such as sugars (Pfau *et al.*, 2016).

The mutualistic interaction with organisms from the genera Rhizobacteria is among the most intricate forms of symbiosis, in which leguminous plants have evolved root nodules that host the bacterial partners and facilitate nutrient exchange (Suzaki, Yoro and Kawaguchi, 2015). These organs grow in response to signalling from bacterial partners present in the rhizosphere, with each plants species having specific rhizobial partners (Xiao *et al.*, 2014). These mutualistic metabolic interactions also confer plants with increased resistance against drought and other stress conditions (Kunert *et al.*, 2016; Staudinger *et al.*, 2016; Vurukonda *et al.*, 2016). Legumes are amongst the most important agricultural crops, including *Glycine max* (soybean) and *Medicago sativa* (alfalfa), since they can replenish organic nitrogen in soils and can improve soil health through their microbial partners (Doran and Zeiss, 2000). Agricultural practices that make use of legumes also reduces reliance on artificial fertilisers. A deeper understanding of the metabolic interactions within the root nodule of legumes could improve the sustainability of agricultural practice.

Since roughly half a plants biomass resides underground, it can be difficult to study without disturbing the plant or rhizosphere. MRI allows to study root systems of live plants non-invasively, and also allows for longitudinal experiments (Ishida, 2000; Van As and van Duynhoven, 2013). Applications include tracking root growth and 3D reconstructed models of root systems (Metzner *et al.*, 2014; Schmittgen *et al.*, 2015; van Dusschoten *et al.*, 2016). Gas exchange in root nodules of *G. max* has also been studied (Macfall *et al.*, 1992; Brown *et al.*, 1997; Chudek *et al.*, 1997). Here, we study root nodules of Medicago truncatula, a model system for root nodulation in legumes which belongs to the same genus as *Medicago sativa* (Barker *et al.*, 1990). Dedicated microcoils for MRM

were developed to obtain *in situ* anatomical images with cellular resolution as well as localised metabolic profiles. MRM and MRS results were then cross-referenced with optical microscopy.

1.4 THESIS SCOPE

Central to the scope of this thesis is the development of MRI applications in *B. braunii* and algae, to answer questions related to food and energy sustainability. To advance the possible applications of MRI in these topics and specimens, a threefold strategy is used. First is the optimisation of pulse sequences on these challenging specimens, including imaging and chemical shift selective pulse sequences, as well as diffusion weighting. Secondly, to develop custom hardware dedicated to specific samples, in the form of microcoils at high and ultra-high field, enabling imaging at cellular resolution. Lastly, by adapting the latest in pulse-sequence designs to microimaging.

In **Chapter 2**, the localisation of hydrocarbons and oils in *B. braunii* var. *showa* is discussed, as well as the two types of colonies which were observed. Diffusion and presence of water channels has been visualised for the first time. In **Chapter 3**, application development for microcoils is examined, and a methodology for testing novel microcoils is introduced. **Chapter 4** presents a practical application of microcoils to study the metabolic profile of *Medicago truncatula* root nodules infected with *Sinorhizobium meliloti*. In **Chapter 5**, the future of micro-imaging and combining diffusion encoding and chemical shift imaging into a DW-CSI is examined, and the potential development of advanced microcoil design is discussed.

1.5 BIBLIOGRAPHY

Aaronson, S. *et al.* (1983) 'Some observations on the green planktonic alga, *Botryococcus braunii* and its bloom form', *Journal of Plankton Research*, 5(5), pp. 693–700. doi: 10.1093/plankt/5.5.693.

Al-Hothaly, K. A. *et al.* (2016) 'The effect of nutrients and environmental conditions on biomass and oil production in *Botryococcus braunii* Race B strains', *European Journal of Phycology*. Taylor & Francis, 51(1), pp. 1–10. doi: 10.1080/09670262.2015.1071875.

Van As, H. and van Duynhoven, J. (2013) 'MRI of plants and foods.', *Journal of magnetic resonance (San Diego, Calif. : 1997)*, 229, pp. 25–34. doi: 10.1016/j.jmr.2012.12.019.

Banerjee, A. *et al.* (2002) 'Botryococcus braunii : A Renewable Source of Hydrocarbons and Other Chemicals', *Critical Reviews in Biotechnology*, 22(3), pp. 245–279. doi: 10.1080/07388550290789513.

Barker, D. G. *et al.* (1990) 'Medicago truncatula, a model plant for studying the molecular genetics of the Rhizobium-legume symbiosis', *Plant Molecular Biology Reporter*, 8(1), pp. 40–49. doi: 10.1007/BF02668879.

Barsch, A. *et al.* (2006) 'GC-MS based metabolite profiling implies three interdependent ways of ammonium assimilation in Medicago truncatula root nodules', *Journal of Biotechnology*, 127(1), pp. 79–83. doi: 10.1016/j.jbiotec.2006.06.007.

Benemann, J. (2013) 'Microalgae for biofuels and animal feeds', *Energies*, 6(11), pp. 5869–5886. doi: 10.3390/en6115869.

Le Bihan, D. *et al.* (2006) 'Artifacts and pitfalls in diffusion MRI.', *Journal of magnetic resonance imaging : JMRI*, 24(3), pp. 478–88. doi: 10.1002/jmri.20683.

Bloch, F. (1946) 'Nuclear Induction', *Physical Review*, 70(7–8), pp. 460–474. doi: 10.1103/PhysRev.70.460.

Bonfante, P. and Genre, A. (2008) 'Plants and arbuscular mycorrhizal fungi: an evolutionary-developmental perspective', *Trends in Plant Science*, 13(9), pp. 492–498. doi: 10.1016/j.tplants.2008.07.001.

Bottomley, P. A. (1987) 'Spatial Localization in NMR Spectroscopy in Vivo', *Annals of the New York Academy of Sciences*, 508(1 Physiological), pp. 333–348. doi: 10.1111/j.1749-6632.1987.tb32915.x.

Boughton, B. A. *et al.* (2016) 'Mass spectrometry imaging for plant biology: a review', *Phytochemistry Reviews*. Springer Netherlands, 15(3), pp. 445–488. doi: 10.1007/s11101-015-9440-2.

Brown, S. M. *et al.* (1997) 'Proton density and apoplastic domains within soybean nodules in relation to the oxygen diffusion barrier', *Plant, Cell and Environment*, 20(8), pp. 1019–1029. doi: 10.1111/j.1365-3040.1997.tb00678.x.

Cabanelas, I. T. D. *et al.* (2015) 'Botryococcus, what to do with it? Effect of nutrient concentration on biorefinery potential', *Algal Research*. Elsevier B.V., 11, pp. 43–49. doi: 10.1016/j.algal.2015.05.009.

Chisti, Y. (2008) 'Biodiesel from microalgae beats bioethanol', *Trends in Biotechnology*, 26(January), pp. 126–131. doi: 10.1016/j.tibtech.2007.12.002.

Chudek, J. A. *et al.* (1997) 'An application of NMR microimaging to investigate nitrogen fixing root nodules', *Magnetic Resonance Imaging*, 15(3), pp. 361–368. doi: 10.1016/S0730-725X(96)00273-1.

Ciobanu, L., Seeber, D. A. and Pennington, C. H. (2002) '3D MR microscopy with resolution 3 : 7 l m by 3 : 3 l m by 3 : 3 l m', *Journal of Magnetic Resonance*, 158, pp. 178–182.

Cornejo-Corona, I. *et al.* (2016) 'Stress responses of the oil-producing green microalga *Botryococcus braunii* Race B', *PeerJ*, 4, p. e2748. doi: 10.7717/peerj.2748.

Demirbas, A. and Fatih Demirbas, M. (2011) 'Importance of algae oil as a source of biodiesel', *Energy Conversion and Management*. Elsevier Ltd, 52(1), pp. 163–170. doi: 10.1016/j.enconman.2010.06.055.

Doran, J. W. and Zeiss, M. R. (2000) 'Soil health and sustainability: managing the biotic component of soil quality', *Applied Soil Ecology*, 15, pp. 3–11. doi: 10.1016/S0929-Get.

van Dusschoten, D. *et al.* (2016) 'Quantitative 3D analysis of plant roots growing in soil using magnetic resonance imaging', *Plant Physiology*, 170(March), p. pp.01388.2015. doi: 10.1104/pp.15.01388.

Ercan, A. E. *et al.* (2015) 'Diffusion-weighted chemical shift imaging of human brain metabolites at 7T', *Magnetic Resonance in Medicine*, 73(6), pp. 2053–2061. doi: 10.1002/mrm.25346.

Eroglu, E. and Melis, A. (2010) 'Extracellular terpenoid hydrocarbon extraction and quantitation from the green microalgae Botryococcus braunii var. Showa', *Bioresource Technology*. Elsevier Ltd, 101(7), pp. 2359–2366. doi: 10.1016/j.biortech.2009.11.043.

Espina Palanco, M., Mogensen, K. B. and Kneipp, K. (2016) 'Raman spectroscopic probing of plant material using SERS', *Journal of Raman Spectroscopy*, 47(2), pp. 156–161. doi: 10.1002/jrs.4768.

Fratila, R. M. and Velders, A. H. (2011) 'Small-volume nuclear magnetic resonance spectroscopy.', *Annual review of analytical chemistry (Palo Alto, Calif.)*, 4, pp. 227–49. doi: 10.1146/annurev-anchem-061010-114024.

Furuhashi, K., Hasegawa, F., *et al.* (2016) 'Effects of culture medium salinity on the hydrocarbon extractability, growth and morphology of Botryococcus braunii', *Biomass and Bioenergy*. Elsevier Ltd, 91, pp. 83–90. doi: 10.1016/j.biombioe.2016.05.007.

Furuhashi, K., Noguchi, T., *et al.* (2016) 'The surface structure of Botryococcus braunii colony prevents the entry of extraction solvents into the colony interior', *Algal Research*. Elsevier B.V., 16, pp. 160–166. doi: 10.1016/j.algal.2016.02.021.

G. Webb, A. (1997) 'Radiofrequency microcoils in magnetic resonance', *Progress in Nuclear Magnetic Resonance Spectroscopy*, 31(1), pp. 1–42. doi: 10.1016/S0079-6565(97)00004-6.

Glover, P. and Mansfield, S. P. (2002) 'Limits to magnetic resonance microscopy', *Reports on Progress in Physics*, 65(10), pp. 1489–1511. doi: 10.1088/0034-4885/65/10/203.

Gouveia, J. D. *et al.* (2017) 'Botryococcus braunii strains compared for biomass productivity, hydrocarbon and carbohydrate content', *Journal of Biotechnology*. Elsevier B.V., 248, pp. 77–86. doi: 10.1016/j.jbiotec.2017.03.008.

Hillen, L. W. *et al.* (1982) 'Hydrocracking of the oils of Botryococcus braunii to transport fuels', *Biotechnology and Bioengineering*, 24(1), pp. 193–205. doi: 10.1002/bit.260240116.

Hoult, D. . and Richards, R. . (1976) 'The signal-to-noise ratio of the nuclear magnetic resonance experiment', *Journal of Magnetic Resonance (1969)*, 24, pp. 71–85. doi: 10.1016/0022-2364(76)90233-X.

Hoult, D. I. (2010) 'The origins and present status of the radio wave controversy in NMR', *Concepts in Magnetic Resonance Part A: Bridging Education and Research*, 34(April), pp. 193–216. doi: 10.1002/cmr.a.20142.

Huang, Z. and Poulter, C. D. (1989) 'Isoshowacene, A C31 hydrocarbon from Botryococcus braunii var. showa', *Phytochemistry*, 28(11), pp. 3043–3046. doi: 10.1016/0031-9422(89)80276-6.

IPCC and Core Writing Team (2014) *Climate Change 2014: Synthesis Report. Contribution of Working Groups I, II and III to the Fifth Assessment Report of the Intergovernmental Panel on Climate Change*. Edited by L. . Meyer and R. K. Pachauri. Geneva, Switzerland.

Ishida, N. (2000) 'The NMR Microscope: a Unique and Promising Tool for Plant Science', *Annals of Botany*, 86(2), pp. 259–278. doi: 10.1006/anbo.2000.1181.

Kandaramath, T., Yaakob, Z. and Binitha, N. N. (2015) 'Aviation biofuel from renewable resources : Routes , opportunities and challenges', *Renewable and Sustainable Energy Reviews*. Elsevier, 42, pp. 1234–1244. doi: 10.1016/j.rser.2014.10.095.

Koo, C. *et al.* (2011) 'A magnetic resonance (MR) microscopy system using a microfluidically cryo-cooled planar coil.', *Lab on a chip*, 11(13), pp. 2197–203. doi: 10.1039/c1lc20056a.

Kovacs, H., Moskau, D. and Spraul, M. (2005) 'Cryogenically cooled probes - A leap in NMR technology', *Progress in Nuclear Magnetic Resonance Spectroscopy*, 46, pp. 131–155. doi: 10.1016/j.pnmrs.2005.03.001.

Kunert, K. J. *et al.* (2016) 'Drought Stress Responses in Soybean Roots and Nodules', *Frontiers in Plant Science*, 7(July), pp. 1–7. doi: 10.3389/fpls.2016.01015.

Levitt, M. H. (2001) *Spin dynamics, Basics of Nuclear Magnetic Resonance*. 1st edn. West Sussex: John Wiley & Sons Inc.

Luypaert, R. *et al.* (2001) 'Diffusion and perfusion MRI: Basic physics', *European Journal of Radiology*, 38(1), pp. 19–27. doi: 10.1016/S0720-048X(01)00286-8.

Macfall, J. S. *et al.* (1992) 'Observation of the Oxygen Diffusion Barrier in Soybean (Glycine Max) Nodules with Magnetic-Resonance Microscopy', *Plant Physiology*, 100, pp. 1691–1697.

Metzger, P. *et al.* (1985) 'Structures of Some Botryococcenes: From the B-Race of the Green Alga Botryococcus Braunii', *Phytochemistry*, 24(12), pp. 2995–3002.

Metzger, P. and Largeau, C. (2005) 'Botryococcus braunii: a rich source for hydrocarbons and related ether lipids.', *Applied microbiology and biotechnology*, 66(5), pp. 486–96. doi: 10.1007/s00253-004-1779-z.

Metzner, R. *et al.* (2014) 'Belowground plant development measured with magnetic resonance imaging (MRI): exploiting the potential for non-invasive trait quantification using sugar beet as a proxy.', *Frontiers in plant science*, 5(September), p. 469. doi: 10.3389/fpls.2014.00469.

Minard, K. R. and Wind, R. a (2001) 'Solenoidal microcoil design - Part II: Optimizing winding parameters for maximum signal-to-noise performance', *Concepts in Magnetic Resonance*, 13, pp. 190–210. doi: 10.1002/cmr.1008.

Nakada, T. (2007) 'Clinical application of high and ultra high-field MRI', *Brain and Development*, 29(6), pp. 325–335. doi: 10.1016/j.braindev.2006.10.005.

Nap, J. P. and Bisseling, T. (1990) 'Developmental biology of a plant-prokaryote symbiosis: The legume root nodule', *Science*, pp. 948–954. doi: 10.1126/science.250.4983.948.

Peck, T. L., Magin, R. L. and Lauterbur, P. C. (1995) 'Design and analysis of microcoils for NMR microscopy.', *Journal of magnetic resonance. Series B*, pp. 114–124. doi: 10.1006/jmrb.1995.1112.

Pfau, T. *et al.* (2016) 'The intertwined metabolism of Medicago truncatula and its nitrogen fixing symbiont Sinorhizobium meliloti elucidated by genome-scale metabolic models.', *bioRxiv*. doi: 10.1101/067348.

Plewes, D. B. and Kucharczyk, W. (2012) 'Physics of MRI: A primer', *Journal of Magnetic Resonance Imaging*, 35(5), pp. 1038–1054. doi: 10.1002/jmri.23642.

Purcell, E. M., Torrey, H. C. and Pound, R. V. (1946) 'Resonance Absorption by Nuclear Magnetic Moments in a Solid', *Physical Review*, 69(1–2), pp. 37–38. doi: 10.1103/PhysRev.69.37.

Sato, Y. *et al.* (2003) 'Biosynthesis of the triterpenoids, botryococcenes and tetramethylsqualene in the B race of Botryococcus braunii via the non-mevalonate pathway', *Tetrahedron Letters*, 44(37), pp. 7035–7037. doi: 10.1016/S0040-4039(03)01784-2.

Schepkin, V. D. (2016) 'Sodium MRI of glioma in animal models at ultrahigh magnetic fields', *NMR in Biomedicine*, 29(2), pp. 175–186. doi: 10.1002/nbm.3347.

Schmittgen, S. *et al.* (2015) 'Magnetic resonance imaging of sugar beet taproots in soil reveals growth reduction and morphological changes during foliar Cercospora beticola infestation', *Journal of Experimental Botany*, 66(18), pp. 5543–5553. doi: 10.1093/jxb/erv109.

Staudinger, C. *et al.* (2016) 'Evidence for a rhizobia-induced drought stress response strategy in Medicago truncatula', *Journal of Proteomics*. The Authors, 136, pp. 202–213. doi: 10.1016/j.jprot.2016.01.006.

Stejskal, E. O. and Tanner, J. E. (1965) 'Spin Diffusion Measurements: Spin Echoes in the Presence of a Time-Dependent Field Gradient', *The Journal of Chemical Physics*, 42(1), p. 288. doi: 10.1063/1.1695690.

Subramanian, R., Lam, M. M. and Webb, A. G. (1998) 'RF microcoil design for practical NMR of mass-limited samples.', *Journal of magnetic resonance (San Diego, Calif. : 1997)*, 133(1), pp. 227–231. doi: 10.1006/jmre.1998.1450.

Sumner, L. W. *et al.* (2014) 'Modern plant metabolomics: advanced natural product gene discoveries, improved technologies, and future prospects.', *Natural product reports*. Royal Society of Chemistry, 00, pp. 1–18. doi: 10.1039/c4np00072b.

Suzaki, T., Yoro, E. and Kawaguchi, M. (2015) *Leguminous Plants: Inventors of Root Nodules to Accommodate Symbiotic Bacteria*, *International Review of Cell and Molecular Biology*. Elsevier Ltd. doi: 10.1016/bs.ircmb.2015.01.004.

Tasić, M. B. *et al.* (2016) 'Botryococcus braunii for biodiesel production', *Renewable and Sustainable Energy Reviews*, 64, pp. 260–270. doi: 10.1016/j.rser.2016.06.009.

Vurukonda, S. S. K. P. *et al.* (2016) 'Enhancement of drought stress tolerance in crops by plant growth promoting rhizobacteria', *Microbiological Research*. Elsevier GmbH., 184, pp. 13–24. doi: 10.1016/j.micres.2015.12.003.

Wake, L. V. and Hillen, L. W. (1980) 'Study of a "bloom" of the oil-rich alga Botryococcus braunii in the Darwin River Reservoir', *Biotechnology and Bioengineering*, XXII(1980), pp. 1637–1656. doi: 10.1002/bit.260220808.

Webb, A. (2012) 'Increasing the sensitivity of magnetic resonance spectroscopy and imaging', *Analytical Chemistry*, 84, pp. 9–16. doi: 10.1021/ac201500v.

Weiger, M. *et al.* (2008) 'NMR microscopy with isotropic resolution of 3.0 μm using dedicated hardware and optimized methods', *Concepts in Magnetic Resonance Part B: Magnetic Resonance Engineering*, 33B(2), pp. 84–93. doi: 10.1002/cmr.b.20112.

Wheeler, D. D. and Conradi, M. S. (2012) 'Practical exercises for learning to construct NMR/MRI probe circuits', *Concepts in Magnetic Resonance Part A: Bridging Education and Research*, 40 A, pp. 1–13. doi: 10.1002/cmr.a.21221.

Xiao, T. T. *et al.* (2014) 'Fate map of Medicago truncatula root nodules', *Development*, 141(18), pp. 3517–3528. doi: 10.1242/dev.110775.

Ye, H. *et al.* (2013) 'MALDI mass spectrometry-assisted molecular imaging of metabolites during nitrogen fixation in the Medicago truncatula-Sinorhizobium meliloti symbiosis', *The Plant Journal*, *75*(1), pp. 130–145. doi: 10.1111/tpj.12191.

Yilmaz, N. and Atmanli, A. (2017) 'Sustainable alternative fuels in aviation', *Energy*. Elsevier Ltd, 140, pp. 1378–1386. doi: 10.1016/j.energy.2017.07.077.